

Sorption enhanced chemical looping gasification of biomass for H₂ and transportation fuel production

Lebohang Gerald Motsoeneng^a, Bilainu Oboirien^{a,*}, Andrea Lanzini^b

^a Department of Chemical Engineering Technology, University of Johannesburg, South Africa

^b Department of Energy, Politecnico Di Torino, Italy

ARTICLE INFO

Keywords:

Gasification
Sorption
Chemical looping
H₂
Fischer Tropsch

ABSTRACT

Sorption-enhanced chemical looping gasification (SECLG) of biomass is a promising process for H₂ and transportation fuel (TF) production at reduced CO₂ emissions and energy penalties. This work demonstrates a comprehensive Lagrange Gibbs Energy Minimization Aspen Plus model for the SECLG of waste bagasse to produce H₂ and TF. The model compares the efficiency of high-performance Nickel Oxide (NiO) and Ferric oxide (Fe₂O₃) oxygen carriers. The influence of parameters including the fuel reactor (FR) temperature, pressure, equivalence ratio, and solid recirculation are examined. Transitory-state pathways of the solid carriers e.g., oxygen carrier and sorbent, during various redox loops, are evaluated. It was found that SECLG can produce syngas with a molar H₂ concentration equal to or greater than 68 % at the lowest FR temperature and pressure of 600 °C and 5 bar. CO₂ in the syngas is significantly limited to substantially less than 10 % of the producer gas. The overall tar yield in the syngas is attainable at low yields within 2×10^{-5} g/kg dry bagasse. The TF yield potential is promising owing to a tunable H₂/CO ratio obtained post a reverse water gas shift phase. Regarding oxygen carrier performance, NiO is more efficient in delivering high-purity H₂ syngas with increased CO₂ sequestration while Fe₂O₃ gains superiority in delivering a producer gas blend with elevated combustibility potentials and a higher TF yield.

1. Introduction

Presently, the industrial production of H₂ and petroleum compounds relies heavily on the conversion of natural gas or lighter hydrocarbons via steam-methane reforming (SMR), auto-thermal reforming (ATR), partial oxidation (PO), and X-to-Fuel technologies that use synthetic gas or oils from gasification or pyrolysis [1,2]. Notwithstanding their proven cross-generational dependency tied to operational efficiencies, these routes harbor intensive CO₂ emissions and thermodynamic inefficiencies owing to the eventual unsustainable nature of the fuel feedstock used e.g., Coal., and the multiple additional units employed for the cleaning and purification of the resultant output [3,4]. Hence, alternative technologies with improved thermodynamic efficiencies coupled with carbon capture and sequestration (CCS) are actively pursued in latent efforts to decarbonize the global energy portfolio and assert carbon neutrality by 2040 [4–6]. One such strategy is the coupling of chemical looping (CL) to both conventional and emerging X-to-Fuel primary-conversion technologies with references to combustion, gasification, reforming, and pyrolysis of biomass [7]. In a broader context, CL

involves splitting chemical reactions into multiple auxiliary reactions facilitated through solid intermediates i.e., Looping material (LM), in intermittent oscillation between their reduced and oxidized (Redox) states [8].

In gasification, this strategy is envisaged to allow for the inherent separation of product streams to eliminate post-stream cleaning, enhancement of process safety by avoiding the direct mixing between lattice O₂ and reductant (e.g. a C_xH_yZ_z), redistribution of the overall heat of reaction to simplify heat integration, the permeation of the thermodynamic equilibrium barrier through a careful selection of redox pairs, catalysts, and the facilitation of individual CL steps at various conditions and chemical state intensities [9]. This is achieved through the recirculation of LM e.g., metal oxide (s) (Me_xO_y) and calcium oxide (CaO), between a gasifier and solid-regenerator operated at temperatures of 600–1200 °C, globally, to enable dynamic REDOX reactions in facilitating the chemical looping gasification (CLG) of fuel residues [10,11]. Reminiscent of these, ideal characteristics of the LM for CL technologies include elevated elemental carrying capacity, recyclability, resistance to attrition, high melting point, adequate heat capacity, high tolerance to

* Corresponding author.

E-mail address: boboirien@uj.ac.za (B. Oboirien).

<https://doi.org/10.1016/j.renene.2025.123022>

Received 27 May 2024; Received in revised form 1 January 2025; Accepted 2 April 2025

Available online 14 April 2025

0960-1481/© 2025 The Authors. Published by Elsevier Ltd. This is an open access article under the CC BY license (<http://creativecommons.org/licenses/by/4.0/>).

contamination and toxicity, cheaper cost, and elevated reactivity potentials, the ability to enable rapid ionic movement, the provision of low resistance to gaseous fusion, and the facilitation of elevated fuel conversion and product selectivity [5,7]. Among adaptations considered, sorption-enhanced chemical looping gasification (SECLG) envisages an effective solution to achieving H_2 production at reduced CO_2 emissions and improved thermodynamic efficiency from in-situ CCS and a characteristically high-quality syngas i.e., with reduced tar and CO_2 content, which eliminates the energy and economic burden normally incurred for the producer gas cleaning and purification [12].

SECLG strategy uses both OC and CaO-sorbent in the same system to achieve high-purity H_2 syngas promoted by near-zero CO_2 concentrations from an inherent CCS [13]. This is shown in Fig. 1.

To date, work on SECLG including that by Refs. [12,14–17], has hinted at possible practical operational thresholds and the thermal self-sufficiency of the adaptation using biomass and coal feedstocks via energy and exergy efficiencies to produce H_2 and electricity and further demonstrated the artificial neural network (ANN) based machine learning optimization strategies of SECLG models. Others including [17], evaluated the economic feasibility of the adaptation to produce H_2 and key-platform alcohols including bio-butanol and pentanol. Additional work has focused on studying the reduction mechanisms of the adaptation using various OC solids including multifunctional looping solid particles e.g. $Ni_xCa_{1-x}O$. Other studies have demonstrated tunable producer gas to produce syngas, pure H_2 , ammonia (NH_3), ethylene, and propylene [18]. While these are substantial in understanding and enhancing the broader mechanisms and benefits of CLG systems, intricacies inherent in model development, and carrier efficiencies, still require further investigation. In this work, we demonstrate an unconstrained Lagrange Multiplier GEM model of SECLG to produce H_2 and Fischer Tropsch (FT) petroleum with near-zero CO_2 emissions from inherent CCS using biomass waste (bagasse) as feed. Within the study, the comparative performance of “high-performance” NiO and Fe_2O_3 -based OCs as well as their thermodynamic transitions and interactions with fuel volatiles, the producer gas, and the enhanced gasification environment are evaluated. Additionally, a Fischer Tropsch model based on the syngas attained from the adaptation is developed and evaluated for transportation fuel production.

2. Materials and methods

2.1. Material and tools

A Thermodynamic H_2 and transportation fuels (TF) production model was developed using the commercial Aspen Plus simulation software. Properties linked to bio-residue characterization were obtained elsewhere [19], while, those of the looping material including the

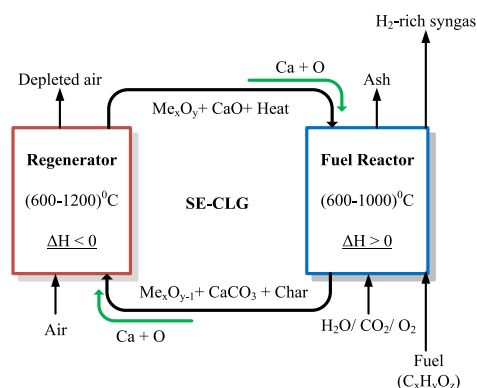


Fig. 1. A redox-based design of experiment approach for SECLG of fuel residues.

Me_xO_y , Me_xO_{y-1} , CaO, and $CaCO_3$ were achieved using the FactSage.8.2 thermochemistry software. Restrictions defined in the gasification and FT blocks were developed using the Simply-Fortran 3 mathematical computing tool. Afterward, the Aspen Plus process modeling software embedded an executable FORTRAN script with FT component distributions and constraints.

2.2. Aspen Plus model

The Peng Robinson-Boston Mathias (PR-BM) Equation of State (EOS) was used as the global method to relate property parameters including the temperature, pressure, and molar volume. Compared to the standard Peng Robinson cubic EOS in Eq (1), PR-BM does not inherently suffer from limitations brought upon by varied systems due to stronger polar interactions, phase behavior of complex associating molecules, and high-accentric factor-based mixtures [20]. As such, global interactions of polar instantaneously volatile and semi-volatile organic compounds emitted from biomass devolatilization, and subsequent FT synthesis are predicted to an acceptable accuracy. A simplified mathematical model for a standardized PR EOS is shown in Eq (1) [21].

$$P = \frac{RT}{V_m - b} - \frac{RT}{V_m - b} - \frac{a\alpha}{V_m^2 + 2bV_m - b^2} \quad \text{Eq 1}$$

Here p – pressure, T – Temperature, R – Universal gas constant, V_m – Molar volume, a – molecular attraction factor, b – molecular repulsion factor, and α – T dependent correction factor.

$$\alpha = \left(1 + m \left(1 - \sqrt{\frac{T}{T_c}}\right)\right)^2 \text{ and } m = 0.37464 + 1.54226\omega - 0.26992\omega^2 \quad \text{Eq 2}$$

An extension within α to account for the temperature and density as shown (2) completes the Boston-Mathias modification.

$$\alpha = \left(1 + m \left(1 - \sqrt{\frac{T}{T_c}}\right)\right)^2 \text{ and } m = 0.37464 + 1.54226\omega - 0.26992\omega^2 \quad \text{Eq 3}$$

Nevertheless, the present model assumes a steady-state operation, instantaneous biomass devolatilization in the FR, intermittent energy flux, a physically consistent state of the Me_xO_y , and hydrocarbons (C_xH_y) potential extrapolated from proximate and ultimate analysis of biomass. Further assertions related to the definition of components include CaO (s), $CaCO_3$ (s), Me_xO_y (s), Me_xO_{y-1} (s), and C(s) as solid components, biomass and ash as non-conventional components, and the remaining intermediates in the product gas, tar, and FT products as conventional components. A tar modeling approach based on a semi-empirical restriction model developed by Ref. [22], for biomass-steam gasification pathways is considered and the possible tar constituents based on the Lagrangian model are shown in Table 1 in supplementary material. While these considerations are given, it is noted that model bias negates biomass's particle size distribution (PSD) and the LM's physical

Table 1
Waste bagasse properties [23].

Ultimate analysis (% db, as received)	
C	46.4
H	6.19
N	0.44
S	0.05
O	44.42
Proximate analysis (% db, as received - except moisture)	
Moisture (MC)	10
Ash	2.5
Volatiles (VM)	79.16
Fixed carbon (FC)	18.13

deterioration.

2.2.1. Material characterization and restrictions

The employed residual biomass properties are shown in Table 1. Similarly, a characterization based on the reductive and regenerative pathways for linked solid state transitions of the LM with the global SECLG temperatures is also shown in Fig. 2.

The HHV of biomass is estimated from the Dulong equation [24].

$$\text{HHV}_{\text{wb,db}} (\text{MJ/kg}) = 0.349C + 1.603H + 0.103S - 0.021O - 0.0005N - 0.021\text{Ash} \quad \text{Eq 4}$$

The predictability of the HHV of biomass using this model is rated at a standard deviation (sd) of $R^2 = 0.98$ for a margin of 0.8 MJ/kg.

Characterization of the LM using the FactSage 8.2. thermochemistry software is shown.

2.2.2. SECLG

The global gasification strategy adopted a Lagrangian Multiplier as a conduit to facilitate Gibbs energy minimization in developing a steady-state thermodynamic environment described in this work. Accordingly, multiple competing reactions occurring at various degrees from miscellaneous balance reactions R8-15 were considered with ease. Further constraints linked to a minimum t_m of 10 °C and the use of a governing EOS were considered. A pool of Aspen Plus components considered is noted (supplementary material) while a detailed Gibbs energy minimization model is shown elsewhere [25]. Nevertheless, a model scenario is presented in Fig. 3.

Waste bagasse and steam (105 °C, 1 bar) are fed to a Fuel reactor

(FR). In Aspen Plus, the FR assumes configurations a, b, and c for linked enhanced-gasification phases. FR a facilitates pyrolysis for biomass devolatilization according to R1 while b and c are for combustion, cracking, reduction, and carbonation by R2 through R6. R2 and R3 are the only exempt reactions in FR b. In FR a, the bagasse residue is decomposed at 700 °C and 5 bar to produce intermediary syngas constituents including C, H₂, N₂, Cl₂, S, O₂, H₂O, and ash. During which, liberation of heat via heat of decomposition (Q_{decomp}) occurs. These products are then sent to FR b where they undergo combustion, reduction, and cracking reactions to produce H₂, CO, CO₂, CH₄, and CH_xO_y. Here, H₂O, Me_xO_y, and CaO are the primary reagents responsible for driving the production of the sub-syngas. After which, the syngas constituents are further reacted in FR c using Me_xO_y and CaO to produce the high-purity H₂ syngas in stream 1. Residual solids i.e., C and ash., along with the reduced LS are then recovered using an Aspen Plus cyclone model (CYCLa) from which, the ash is purged, and residual C and the LM are fed to the CR.

The FR is operated at 700 °C and 1 bar. An equivalence ratio (ER) of 0.5 amu is used while CaO and Me_xO_y distributions at LS/biomass (b) of 0.5 amu. It is noted that while these prefixed operational conditions are employed, a comprehensive sensitivity study facilitated by equation (1) through 10, is shown elsewhere. Nevertheless, the reduced LS i.e., CaCO₃ and Me_xO_{y-1}, and residual C are fed to a calciner reactor (CR) that is operated at 900 °C and 1 bar. Here the CaCO₃ is thermally dissociated to produce CaO and CO₂ as shown in R6. The desorption mechanisms for CO₂ are comprehensively described by Ref. [26]. The CR products including the Me_xO_{y-1} and carbon are subsequently fed to an air reactor (AR) operated at 900 °C and 1 bar. During this, low

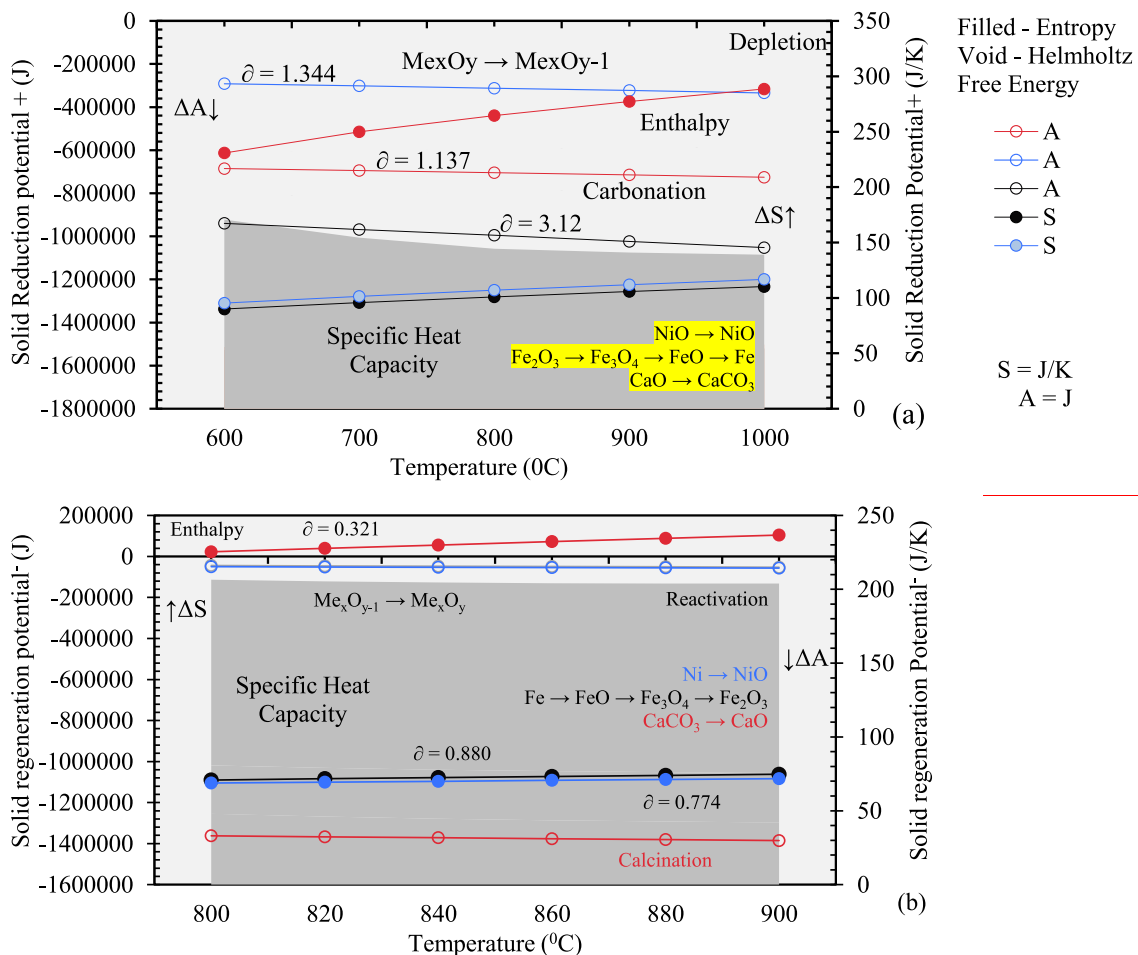


Fig. 2. LS REDOX evolution with temperature in a) FR during reduction and b) CR-AR during regeneration.

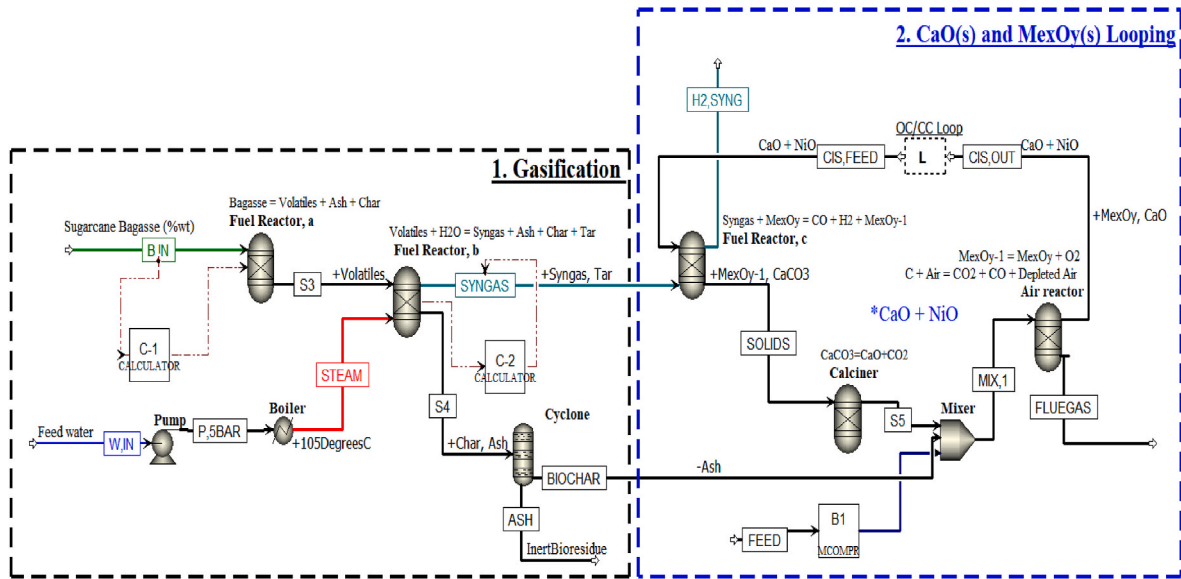


Fig. 3. Enhanced gasification model for high-purity H₂ syngas recovery.

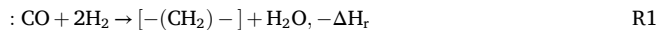
population density air comprising 0.21 O₂ and 0.79 N₂ is fed 100 kg/h air for 22.4 mol Me_xO_y. Here, R5 and R7 occur for Me_xO_y regeneration and residual carbon combustion (RCC). From the AR, the regenerated OC, decoupled CO₂, and RCC CO₂ within a depleted air stream are recovered.

2.2.3. FT model

FT synthesis occurs via methane steam reforming (MSR), reverse water gas shift (RWGS), FT synthesis, and subsequent purification. Primarily, The H₂-rich syngas stream i.e., crude H₂., from SECLG of biomass at 700 °C and 5 bars is cooled using an Aspen Plus heat exchanger model operated at 300 °C. The conditioned gas is then sent for MSR. Here, CH₄ in the syngas S16 is converted to more H₂ and CO at 350 °C and 20 bar as shown in R20. Owing to the abundance of CO₂ in the flue gas, this is followed by a reverse WGS linked to Xu and Froment kinetic equations comprehensively described elsewhere [27]. Here, CO₂ is reacted with H₂O_(v) to compensate for the low levels of CO recovered in the syngas for a subsequent FT step shown in Fig. 4.

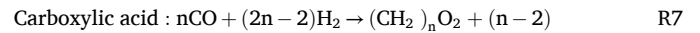
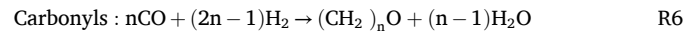
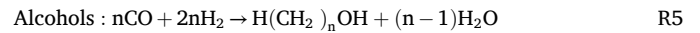
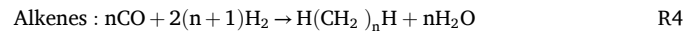
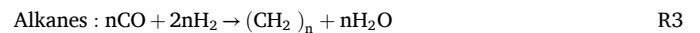
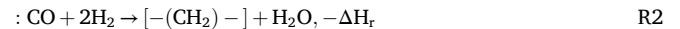
In principle, multiple competing reactions i.e., R1–R7., occurring at various degrees are possible during FT synthesis [28].

Straight – chained Olefins and paraffins



R1 and R2 represent the general FT synthesis reaction scheme where $-(\text{CH}_2)-$ outlines the synthesized liquid petroleum from the notably, highly exothermic process $(-\Delta H)$ with enthalpies sub-seceding up to 170 kJ/mol.

Straight – chained Olefins and paraffins



A fixed conversion FT reactor model in Aspen Plus fitted with a FORTRAN-based ASF distribution was employed for TF production. Further constraints consider an FT reactor operated at 200–350 °C during a low-temperature FT synthesis. The product stream is then sent to a subsequent purification train comprised of a flash and PETROFRAC column to remove residual gases and H₂O_(v).

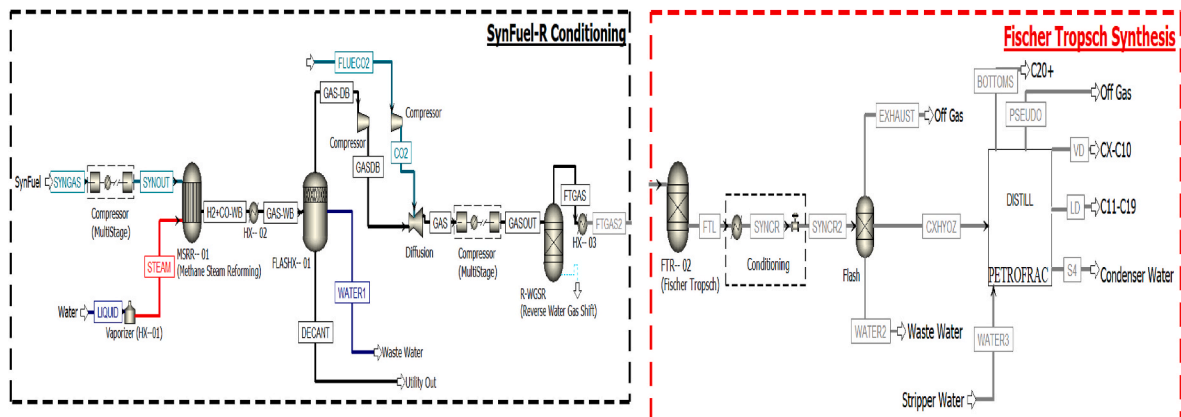


Fig. 4. FT production.

2.3. Balances and performance analysis

The mass and energy balances are described by Eq(s) 5 and 6.

$$\Sigma m_{in} = \Sigma m_{out} \quad \text{Eq 5}$$

$$\Sigma E_{in} = \Sigma E_{out} \quad \text{Eq 6}$$

The control volume applicable to each balance varies. The corresponding factual balances for the FR, CR and AR are presented through 7–9, respectively.

$$m_b + m_{H_2O} + m_{CaO} + m_{Me_xO_y} \rightarrow m_{(H_2+CO+CO_2+C_xH_y)} + m_c + m_{tar} + m_{ash} + m_{CaCO_3} + m_{Me_xO_{y-1}} \quad \text{Eq 7}$$

$$m_{CaCO_3} \rightarrow m_{CaO} + m_{CO_2} \quad \text{Eq 8}$$

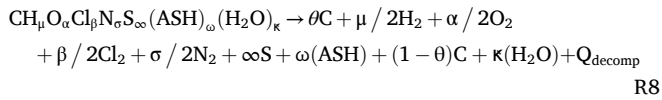
$$m_{Me_xO_{y-1}} + m_{O_2} \rightarrow m_{Me_xO_y} \quad \text{Eq 9}$$

$$m_c + m_{O_2} \rightarrow m_{CO_2} + m_{CO} \quad \text{Eq 10}$$

$$E_{pump} + E_{HX} + E_{FR} + E_{CR} + E_{AR} + E_{cyclone} \rightarrow E_{lost (ash+heat)} + E_{syn} + E_{syn} + E_{flu} \quad \text{Eq 11}$$

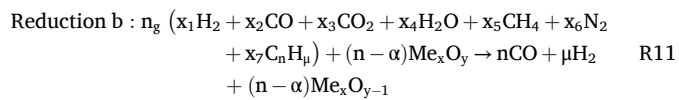
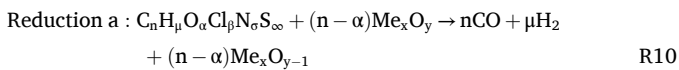
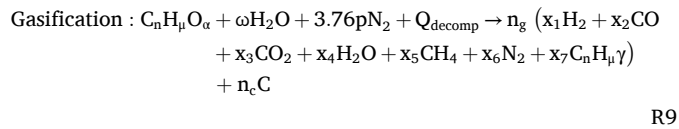
2.4. Auxiliary reactor balances

In the near absence of O_2 or H_2O , biomass devolatilization in the FR occurs via R1 [29].

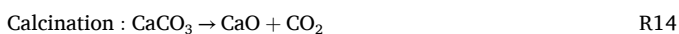
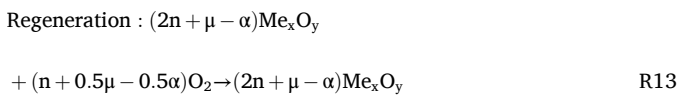


In R8, θ and Q_{decomp} is the carbon conversion and the heat of biomass decomposition, respectively. R8 is facilitated by a FORTRAN script derived from the Proximate, Ultimate, and Sulfur characterization of bagasse biomass shown elsewhere.

Following R8, innate enhanced gasification in FR is described by R9–12.



However, during R9, multiple sub-reactions linked gas shift, carbon reduction and combustion described elsewhere occur [30]. The regeneration of LS is facilitated by R13 and R14 in the AR and CR, respectively, while a further air promoted residual carbon combustion (RCC) R8 in AR occurs.



2.5. Performance evaluation

Enhanced gasification feed balances including the equivalence ratio (ER) and solid recirculation (SR) i.e., carbonation ratio (CR) and the reduction ratio (RR), are given by Eq (12)–(14).

$$ER = \left(\frac{m_{H_2O}}{m_{biomass}} \right) \quad \text{Eq 12}$$

$$CR = \left(\frac{m_{CaO(fs)}}{m_{biomass} + m_{CaO(rs)}} \right) \quad \text{Eq 13}$$

$$RR = \left(\frac{m_{Me_xO_y(fs)}}{m_{biomass} + m_{Me_xO_y(rs)}} \right) \quad \text{Eq 14}$$

Here fs – feed solid and rs – reduced solid.

The gross (GHV) and net heating (NHV) values are determined as follows.

$$GHV (\text{cal / gm}) = HHV_{syn} (1 - mc_{syn} / 100) \quad \text{Eq 15}$$

$$NHV (\text{cal / gm}) = (GHV - Q_{Latent \text{ vaporization of } H_2O}) \quad \text{Eq 16}$$

Here mc-moisture content, gm – grams per 1000, cal – calories and syn – synfuel.

The cold (CGE) and hot gas (HGE) efficiencies are determined as follows.

$$CGE = \frac{HHV_{syn}}{HHV_{biomass}} \quad \text{Eq 17}$$

$$HGE = \frac{HHV_{syn} + Q_{Sensible, syn}}{HHV_{biomass}} \quad \text{Eq 18}$$

Here $Q_{Sensible, syn} = \sum m_{syn} \times C_{p, syn} \times (T^{syn} - 298)$ and, HHV – Higher Heating Value.

Carbon conversion (θ) is determined as follows.

$$\theta_c = \frac{\sum \left(\frac{12n_{C_i}}{mw_i} \times m_i \right)}{C_{biomass}} \quad \text{Eq 19}$$

Here i – carbon bearing species with n – number of carbon atoms and mw – Molecular weight.

Other performance indicators including the product selectivity, and the $C_xH_yO_z$ availability were determined as follows.

$$S \text{ selectivity (amu)} = FTL_{out} / m_{total} \quad \text{Eq 20}$$

$$C_xH_yO_z \text{ (amu)} = C_xH_yO_{z(total)} - \text{impurities} \quad \text{Eq 21}$$

Here FTL – Fischer Tropsch liquid, m – material flow.

3. Results and discussion

3.1. Model validation

The present model covers gasification, CL, calcination, Me_xO_y regeneration, RCC, H_2 , and FT synthesis. Such grounds for model validation considered a gasification phase in the FR fitted with experimental and simulated steam gasification work reported in the literature [30, 31]. Additionally, H_2 and FT synthesis developed in this work adopt approaches based on simulation and experiments described in work by Refs. [28,32,33], respectively. It is noted that while the present study introduces an unconstrained Langrange multiplier Gibbs energy

minimization approach, a consensus for CL development and integration is shown elsewhere [12,16].

3.2. Thermodynamic modeling of SECLG

3.2.1. A performance evaluation of LS during enhanced gasification

A parametric study assessed the performance of NiO and Fe_2O_3 OCs in SECLG to produce high-purity H_2 . These are referred to as scenarios 1 and 2, respectively. The parameters used include the FR temperature, FR pressure, ER, and SR. These were evaluated at 600–1000 °C, 1–11 bar, 0.2–1 amu CaO/b, 1–2 amu H_2O /b, and 2.2–4.2 atomic mass unit (amu) OC/b, respectively. Results from a sensitivity study are shown in Fig. 5.

3.2.1.1. The effects of the FR temperature. The effects of the FR temperature on the presented scenarios are shown in Fig. 5a. While scenario 1 is observed to have an overall increase in H_2 production with the FR temperature at 0.698–0.703 for 600–1000 °C, respectively, scenario 2 exhibits a converse relationship with the H_2 yield significantly reduced at 0.68–0.625 for 600–1000 °C. Moreover, the H_2 recovery via scenario 1 is consistently superior to that from scenario 2 during this period. Notwithstanding the readily perceived influence of the different OCs employed, the observed relationship for H_2 yield with the FR temperature may be better explained by the thermodynamic characterization of the different OCs used (Fig. 2). It is observed in Fig. 2 that the overall Helmholtz Free Energy (ΔA) and entropy (ΔS) in both scenarios increase with the FR temperature as related to the above-stated relationship. For the evaluated FR temperatures at 600–1000 °C, NiO consistently has the highest ΔA potential as compared to Fe_2O_3 . In fact, in line with the FR initial and endpoint temperatures assessed, these are at (−268954.1, −304351.7) J versus (−685196.1, −975355) J, respectively. This would as such, explain the above-stated relationships i.e., increasing H_2 yield and NiO H_2 production superiority over Fe_2O_3 with the FR temperature., as the higher the ΔA , the more lattice O_2 release is favored [34,35]. Consequently, abundant lattice O_2 decoupling from H_2O along with any compatible O_2 -vector for effective collisions or interactions is favored. Hence, a consistently superior H_2 yield in scenario 1 is observed as compared to that in scenario 2. While the present analysis bases the ΔA with the FR temperature and volume as the natural variables to combine

both the internal energy (ΔU) and ΔS contributions, other literature e.g., a study by Ref. [36], evaluated similar relations using the Gibbs free energy (ΔG). Nonetheless, NiO's capacity as a known catalyst for high-temperature systems might have also contributed to the above-reported observations [37,38].

Similar observations to the ones indicated in this work i.e., for increasing H_2 with the FR temperature., are also reported elsewhere [12, 17]. Here, [12], investigated the thermodynamic performance of an autothermal SECLG to produce H_2 and electric power. In this work, NiO and CaO were used as OC and CC, respectively in Aspen Plus FR models operated at 600–740 °C. It was observed that in this FR temperature range, the H_2 in the syngas decreased with the FR temperature. Elsewhere, [17], evaluated the economic feasibility for SECLG of lignocellulosic biomass to produce butanol and pentanol. Fe_2O_3 and CaO were used as OC and CC, respectively. Among the parameters considered, the H_2 yield was evaluated at 200–1000 °C. It was observed that during this period, H_2 was decreasing with the FR temperature. Nevertheless, the overall reduction in H_2 with the FR temperature in scenario 2 may also similarly be owed to the thermodynamic properties of Fe_2O_3 at high temperatures which might instigate a shift in the chemical reaction equilibrium (CRE). This observation is similar to the findings by Refs. [16,39].

Amongst these, [16], evaluated the thermodynamic performance of SECLG with coal as fuel to produce H_2 -rich syngas using an Aspen Plus FR model for temperatures at 500–1000 °C. This work employed Fe_2O_3 and CaO as OC and sorbent, respectively. It was found that overall the H_2 production in syngas was in fact, decreasing with the FR temperature at 5–3.5 kmol/h for 500–1000 °C. [39], proceeded to experimentally evaluate the CLG of pine wood biomass using a synthetic Fe_2O_3 -based OC in a 1.5kW_{th} continuous unit. Al_2O_3 was used as support for the FR temperature, ER, and O_2 /b ratio of 820–940 °C, 0.05–0.65, and 0.2–0.6, respectively. Among the syngas constituents, it was also found that H_2 was steadily decreasing with FR temperature. However, understanding the in-depth behavior linked to the performance of Fe_2O_3 OC in high-temperature gasification systems will require further experimental studies.

CO_2 in the product gas is significantly limited to <10 % of the product gas in both scenarios. This may be due to efficient carbon capture

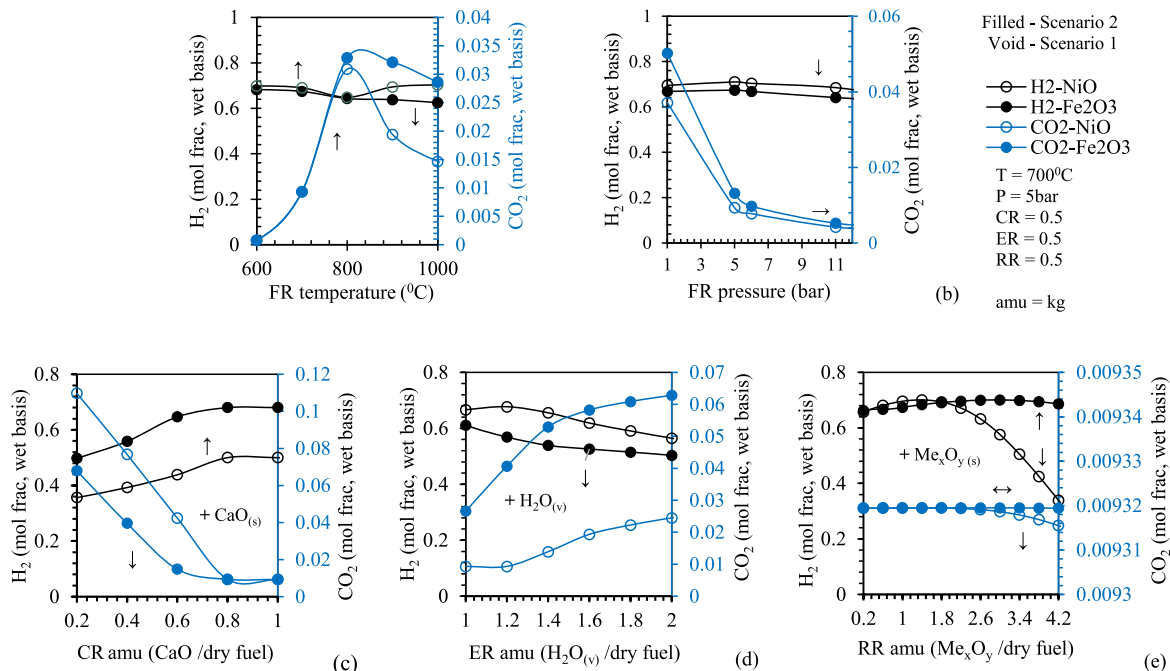


Fig. 5. Surface degrees of freedom (SDoFs) on H_2 production and CO_2 sequestration with the a) FR Temperature b) FR Pressure c) CR d) ER and e) RR.

through R12 which would significantly reduce CO₂ concentrations in the product gas as compared to conventional gasification systems [40]. However, the overall CO₂ sequestration decreases from a near-zero shared molar fraction at 600 °C to 0.0147 and 0.0286 for scenarios 1 and 2, respectively, at 1000 °C. This observation is also noted in a related study by Ref. [12]. A possible explanation may be due to reduced CO₂ synthesis kinetics at low temperatures in a SECLG system. This observation may additionally hint at optimal calcination temperatures by the support CaO at 600–800 °C. Nonetheless, the catalytic effects of both OCs employed in separate scenarios may also have played significant roles in the above-stated observations. Similar findings for limited CO₂ in the producer syngas for SECLG are also reported elsewhere [12, 41]. Among these, [41], evaluated a thermodynamic integrated sorption-enhanced staged-gasification of biomass and in-situ CO₂ utilization by MR. It was observed that the CO₂ was severely limited to 2.1 % by volume of the producer syngas.

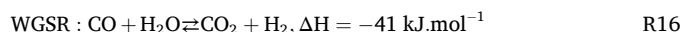
At 600–800 °C, H₂ decreases while CO₂ increases in both scenarios. This reaches break-even at 800 °C with H₂ yield at 0.65 in both scenarios while CO₂ remains slightly differentiated at 3.08 and 3.28 % moles of the product gas for scenarios 1 and 2, respectively. This may be due to a shift in CRE in both scenarios as after the break-even, CO₂ production reaches a state of constant inclination until a temperature of 1000 °C. However, further studies dedicated to catalysis are needed to understand more about the reaction kinetics of enhanced gasification with temperature.

3.2.1.2. The effects of the FR pressure. The results obtained for the effects of the FR pressure on enhanced gasification are presented in Fig. 5b). An overall decrease in H₂ and CO₂ yield in both scenarios is observed from 1 to 11 bar. During which, H₂ increases from an initial FR pressure of 1 bar, reaches break-even at 5 bars, then, constantly decreases to 11 bars. As with the reported effects of FR temperature on the broad gasification kinetics, this lack of consistency in H₂ yield with the FR pressure may be a result of a shift in the CRE which would favor the production of other syngas constituents namely CO₂, CO, H₂O, and C_xH_y. R1–R8 to validate this assertion are shown. It is additionally, noted that similar observations related to a CRE shift indication, are reported in a related study by Ref. [12]. However, contradicting observations are also reported in a study by Ref. [12] while other studies with references to that by Ref. [16] have not shown the H₂ response to the change in the FR pressure. In this study by Ref. [12], the overall H₂ yield in the producer gas is observed to increase for 1–20 bar for a linked SECLG configuration under a NiO OC. Nonetheless, scenario 1 maintains a steady H₂ yield superiority over scenario 2 during this period i.e., 1–11 bar. This may be due to the different OCs employed which would facilitate enhanced gasification at various rates and intensities. Unlike with the FR temperature, the effects of the Me_xO_y reduction with pressure on changes in the thermodynamic properties with references to the ΔS and ΔA were not observed for FR pressures of 1–11 bar in the FactSage thermochemistry software's Me_xO_y to Me_xO_{y-1} characterization. Nevertheless, NiO as an OC in scenario 1 is observed to be more effective in enhancing H₂ output in the product gas than Fe₂O₃ in scenario 2.

Elsewhere, CO₂ sequestration increases for 1–11 bars in both scenarios. During this period, CO₂ initially reduces rapidly for 1–5 bar then, steadily until 11 bars. This may also be a result of reduced enhanced gasification reaction kinetics which would ultimately lead to less CO₂ production with FR pressure. As such, CO₂ recovery in the product gas reduces with the FR pressure. This observation is entirely consistent with findings from a thermodynamic modelling study of SECLG by Ref. [12]. Here, CO₂ recovery in the product gas is observed to decrease from a FR pressure of 1–20 bar. Moreover, the eventual performance of both OCs is almost consistent with scenarios 1 and 2 achieving CO₂ outputs of 0.0052 and 0.0042 at 11 bars. In resonance with the analysis of the performance of the employed OCs in the described scenarios, NiO is observed to be a more efficient OC for high-purity H₂ production as

compared to Fe₂O₃. However, the capacity for both OCs to produce high-purity H₂ at reduced pressures is promising for enhancing present H₂ production pathways. These observations i.e., for the effects of the FR pressure on H₂ and CO₂ yields could additionally hint at CaO's CO₂ sequestration efficacy at reduced pressures within 5 bar for any Me_xO_y employed.

3.2.1.3. The effects of the ER. Infamous for affecting the performance of high-temperature reaction systems through the syngas-specific weight, carbon conversion, gas heating value, and lineated efficiencies, the effects of the ER were evaluated at 1–2 amu H₂O/b as shown in Fig. 5c. Other related studies have reported lower and higher ER ranges at 0.2–4 amu b/gasifying agent [12,16]. Nonetheless, an increase in the ER results in an overall decrease in H₂ recovery with a simultaneous increase in CO₂ in the producer gas in both scenarios. Scenario 1 linked to the use of NiO as an OC is observed to initially have a steady increase in H₂ production with H₂O_(v) from 0.66 to 0.68 at ER of 1–1.2. This is followed by a maintained decrease in H₂ until an ER of 2. Scenario 2, however, maintains a steady decline in H₂ production with an increase in ER. The above-described behavior in scenario 1 during the initial phase at ER of 1–1.2 is likely due to a WGSR which converts CO using H₂O_(v) to produce more H₂ and by CO₂ gas.



While this was expected, an overall decrease in H₂ with ER in both scenarios might have, however, been due to an equilibrium shift during R16 which would ultimately reverse the reaction to favor the production of H₂O instead [42–44]. Among these, a study by Ref. [42], investigated the Influence of ER during gasification in a pilot scale fixed bed gasifier for 50 kg/h gas yield. In this work, pine wood block and corn stalk briquette were converted in a FR operated at ERs >0.1 amu. In was observed that the gas yield fluctuated with varied ER such that too high and too low ERs resulted in excess gasification and, incomplete gasification, respectively. These would then lead to product quality attainment inefficiency.

For the case of carbon-capture, CO₂ increases with ER for 1–2 amu H₂O/b. Unlike the observation incurred for H₂ production in the present model, this is a typical result of a forward WGSR to produce more CO₂ and H₂ with the addition of a gasifying agent. It however noted that, contrary to the observed H₂ production, the sustained typical behavior of CO₂ may be due to the notably low levels of CO₂ reported in this work. Consequently, while a shift in the reaction direction would favor the reduction of H₂, the models already produce an insignificant amount of CO₂ which would submit to the pre-described alteration. This observation i.e., Increase CO₂ with ER, is noted in related work by Refs. [13,16]. Results from a study by Ref. [45] further indicate a similar relationship for CO₂ recovery with the addition of a gasifying agent. Here, CO₂ was used as a gasifying agent in a SECLG equilibrium model. It was observed that for an ER of 0–0.5 amu, CO₂ in the product gas was in fact increasing with the ER of 0–0.5 amu. It is further noted that while increasing the ER would typically broadly enhance the gasification efficiency, striking the right balance between steam and biomass quantities used is essential in delivering high-quality product gas.

3.2.1.4. The effects of the CR. The effects of CaO were evaluated at CR ratios of 0.2–1 amu as shown in Fig. 5d. An evaluation approach for the CR is given in Eq (40). It is observed that an increase in CR results in an overall increase in H₂ production with a concomitant CO₂ sequestration in both scenarios. This is due to an elevated amount of CaO available to sequester CO₂ to therefore promote enhanced H₂ production in both scenarios. This behavior is entirely consistent with results reported in work related to the use of CaO as a chemical sorbent in high-temperature systems [16,46]. A study by Ref. [16], evaluated the thermodynamic performance of SECLG to produce H₂-rich syngas. Coal was used as fuel in an Aspen Plus FR Model. Among a pool of parameters considered, the

CR was evaluated at 0.2–1.3 amu CaO/C. It was observed that H_2 increased at 3.5–5.5 kmol/h while CO_2 decreased at 3–0.1 kmol/h for CaO/C range of 0.2–1.3 amu CaO/C. Another study by Ref. [46], evaluated the SECLG of rice straw in a U-shaped fixed bed gasifier. The gasifier was operated at 600–850 °C with Fe_2O_3 and CaO as the LM. It was observed that an increase in CaO/C increased H_2 yield and CO_2 sequestration.

For the CR range of 0.2–1 amu, scenario 1 is observed to almost consistently have lower H_2 , and higher CO_2 concentrations as compared to scenario 2. Despite the influence of the different OCs employed, this may be due to a reduced amount of NiO due to a tradeoff balance from CaO addition. As such, less amount of NiO is available to catalyze the production of H_2 in scenario 1 as compared to 2. Moreover, this observation may hint at the ability of Fe_2O_3 to maintain a consistent OC and catalysis performance at low concentrations as compared to NiO. However, these assertions should be subject to dispute or validation from other studies.

3.2.1.5. The effects of the RR. The effects of the RR were evaluated at 0.2–4.2 amu Me_xO_y/b as shown in Fig. 5e while the RR evaluation approach is indicated in Eq. (10). The overall H_2 production is observed to decrease in scenario 1 while increasing in scenario 2 from an RR of 0.2–4.2. During which, H_2 in scenario 1 decreases at 0.66–0.34. It is further noted that during this period, H_2 initially peaks at 0.701 then decreases rapidly to 0.339 for RR of 1.4 and 4.2, respectively. These observations are similar to the results reported in work by Refs. [16,45]. Here, the researchers employed Fe_2O_3 as an OC in varying SECLG cases. It was observed that for linked scenarios, H_2 in the product gas was decreasing with the RR. Scenario 2, however, maintains a consistent increase in H_2 production at 0.663–0.686 for RR at 0.2–4.2. This may be due to the thermodynamic behavior of the different OCs used in the respective scenarios. This may further hint at optimal OC i.e., NiO and Fe_2O_3 , concentrations for efficient H_2 recovery during SECLG. However, the influence of RR on the H_2 synthesis for Fe_2O_3 reported in work by Ref. [16], differs from the one reported in this work. Here, coal was used as fuel in a constrained SECLG GEM system operated within RR of 3.5 amu. In this study H_2 decreases for RR of 0.2–1.6 while in the present work, the H_2 is observed to increase during this period. It is asserted that the feedstock used during the SECLG of carbon residues might also play

a significant role in the performance analysis of these systems from which the extent of various reduction mechanisms may differ.

However, CO_2 is observed to decrease steadily with RR in both scenarios. The addition of Me_xO_y is observed to have minimal impact on CO_2 synthesis for RR of 0.2–4.2. This observation is similar to results reported in work by Ref. [16]. Here, the CO_2 recovered in the product gas is slightly differentiated for RR of 0.2–2 amu. However, a study by Ref. [45], investigated extended RR ranges of 0.2–20 amu. It is noted from this study that while the effect of RR within the ranges reported in this work and the study by Ref. [16], is observed to have minimal impact on the H_2 production, RR above 5 amu indicates a steeply increasing CO_2 recovery in the product gas. However, with cc being a factor in this work, extending RR ranges above 5 would not be ideal.

3.2.2. Producer gas quality

An evaluation of the producer gas quality through the tar formation, gas composition, and energy content of the syngas i.e., GHV and NHV., is presented in Fig. 6. Further efficiencies including the CGE and HGE are evaluated. A tar modelling approach inclusive of tar derivatives considered is shown elsewhere (Table 1).

3.2.2.1. Gas composition. The producer tar is given by CH_xO_y . Here the parameters (x, y) are temperature-dependent variables. A distribution of observed tar components in the producer syngas is shown in Fig. 6b. The overall tar yield in the present scenarios is attained at low yields within 2×10^{-5} g/kg dry bagasse. This represents way less than 1 % of the syngas formed. This may be due to possible tar reductive pathways by the employed LS during CL. A recent study by Ref. [47], evaluated clean syngas synthesis from a CLG of pine forest residue. In this work, a pilot 20kW_{th} pilot plant was used with $FeTiO_3$ from ilmenite as Fe_2O_3 vector material. A tar analysis shown further compared the results of a lineated 1.5 kW_{th} pilot scale CLG [8]. The results revealed a producer tar with benzene, toluene, naphthalene, and acenaphthylene as dominant constituents whilst the remaining with references to lineated isomers and planar polycyclic aromatic hydrocarbon e.g., fluorene., were in almost negligible quantities. The aggregate tar potential comprised roughly 0.001 of dry biomass residue. As a result, the tar in the syngas was significantly reduced. In this work, butane and ethane had the highest abundance as compared to naphthalene, phenanthrene, catechol,

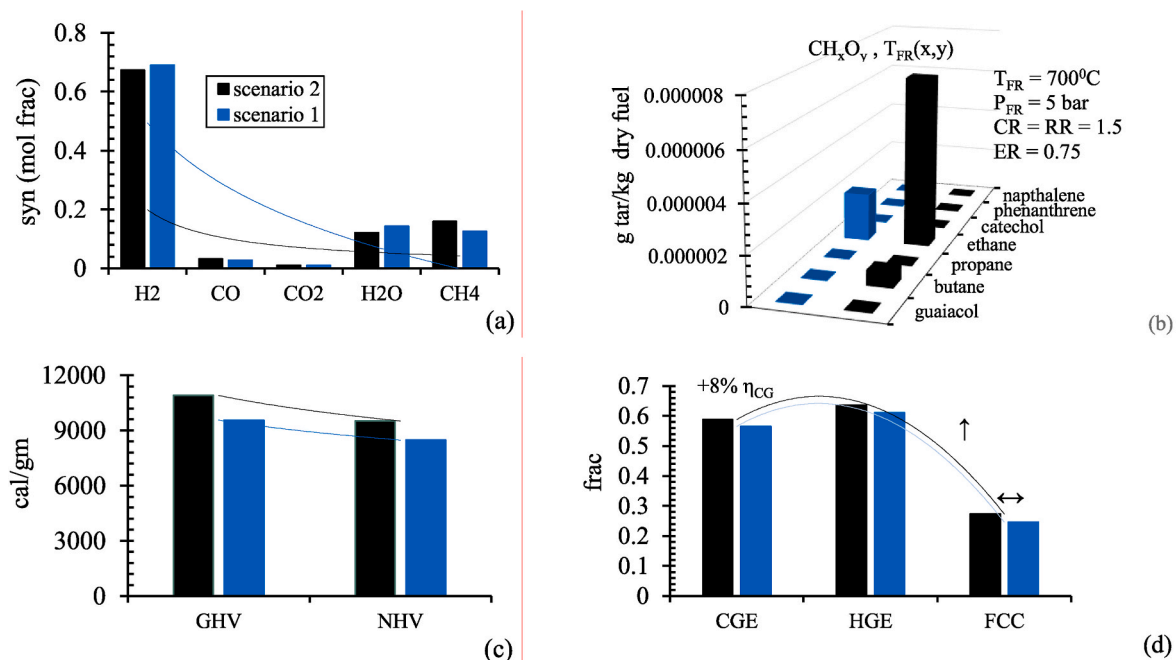


Fig. 6. Fixed-point product syngas quality via the a) Syn-composition b) Tar mapping c) Energy content and d) Gas efficiency.

propane, and guaiacol. These latter tar derivatives are relatively negligible in quantity. It is noted that with favorable gasification kinetics promoted by elevated FR temperatures and pressures, such tar derivatives like naphthalene could be further cracked into lineated vapor subsets [48,49]. Hence, a severely reduced tar concentration in the eventual product output. Moreover, tar synthesis is entirely dependent on the type of fuel feedstock used owing to the varying proportions of bio-constituents with references to cellulose, hemicellulose, and lignin constituents [50]. As such, while the model reasonably accounts for other parameters which have an impact on tar formation including the feed rate, gasifying agent, associated ER, and the proxanal, ultanal and sulfanal characteristics, this study acknowledges the negation of a modeling bias associated with the inclusion of such biomass properties to affect the tar formation during enhanced gasification.

Elsewhere, the resulting syngas composition post-SECLG is indicated in Fig. 6a. While other syngas constituents including H_2S and C_xH_y were considered in the Aspen Plus FR models, they are considered negligible due to their apparent yields of $\ll 0.1\%$ of the producer gas. The H_2 recovery in the producer gas is elevated at ≥ 0.6 by moles of the producer syngas in both scenarios as compared to conventional gasification [51,52], unassisted CLG [53,54] and SEG technologies [55,56], regardless of the gasifying agents or LS employed. This reinforces the SECLG's potential as a technological candidate for green H_2 production with minimal CO_2 emissions. Further notable syngas characteristics include elevated CH_4 and H_2O yields as compared to CO_2 and CO . These i.e., CH_4 and H_2O , roughly make up < 0.4 by molar fraction of the syngas in both scenarios.

In terms of OC performance, the tar recovered in scenario 2 is higher than that in scenario 1. As such, NiO as an OC material in enhanced SLG is generally most likely to limit the tar production in enhanced gasification technologies regardless of the fuel feedstock as compared to Fe_2O_3 . It is however noted that due to a reasonably close margin in the eventual product gas tar, both OCs demonstrate the highest potential for reducing tar synthesis and improving the commercial benefit of enhanced gasification technologies. Moreover, both OC materials produce a high purity i.e., 0.6 M, H_2 syngas with limited CO_x emissions.

3.2.2.2. Gas combustibility. A further reference to the producer syngas quality in the developed scenarios considers the gross and net combustion potentials i.e., GHC (Eq (9)) and NHV (Eq (10)). Additionally, lineated efficiencies i.e., CGE and HGE and FCC are shown in Fig. 6b. At least 8480.53 cal per gm as minimum energy is embodied in the producer syngas for each scenario. Ultimately, the producer gas in both scenarios is effectively, and readily combustible [57]. It is further noted that this value is on a wet basis for GHV [58]. In terms of combustibility, the producer syngas in scenario 2 maintains superiority over that in scenario 1. This is due to the elevated GHV and NHV of 10900.77 and 9567.06 cal/gm respectively, in scenario 2 as compared to 9567.06 and 8480.53 cal/gm in scenario 1. Moreover, the lineated CGE and CGE of 58.8 and 63.5 % in scenario 2 are greater than that at 56.5 and 61.1 % in scenario 1. Since at this point determination, the H_2 content in scenario 1 is higher than that in scenario 2 at 0.69 versus 0.674, respectively, this is indicative of a higher combustible C_xH_y vapors yield in scenario 2 as compared to 1. In fact, CH_4 in scenario 2 is higher at 0.2 as compared to that of 0.1 in scenario 1. Due to this observation, it is no surprise that the FCC in scenario 2 is higher at 27.3 % as compared to that of 24.6 % in scenario 1. A further H_2 -C tradeoff in the producer syngas quality is observed with slightly higher CO and CO_2 yields in scenario 2 as compared to 1.

However, while the combustibility potential of the producer syngas in the observed scenarios is reasonably optimal for recovering a readily combustible blend fuel, the FCC at this temperature could be improved. In terms of the syngas quality, both scenarios outline the highest potential for producing high-purity syngas with elevated H_2 content with optimal combustion efficiency. In terms of OC performance, NiO is most

effective in delivering superior H_2 -rich syngas while Fe_2O_3 is most effective in delivering the most combustible syngas.

3.3. LM evolution in FR

While certain reducibility pathways are comprehensively described elsewhere in the literature [59–61], the present work evaluates a mass-based degree of reduction (DR^+) of the LM with the FR temperature and pressure. The DR^+ for the LM in the FR was evaluated at FR temperatures and pressures of 600–1000 °C and 1–6 bar, respectively. The reduction potentials are shown in Fig. 7.

The DR^+ signifies optimal FR thermodynamic operational thresholds to achieve maximum H_2 output and thermal efficiency. Owing to differences in mass balances between the stable forms (SF) and their depleted states (DF), the maximum DR^+ is at 0.786 Ni, 0.90 FeO, and 1 CaCO_3 for NiO, Fe_2O_3 , and CaO. A temperature and pressure-dependent linear reductive pathway of $\text{Fe}_2\text{O}_3 \rightarrow \text{Fe}_3\text{O}_4 \rightarrow \text{FeO} \rightarrow \text{Fe}$ for Fe_2O_3 is deduced while direct-reductive pathways for Ni and CaCO_3 , respectively are asserted. It is noted that the Fe_2O_3 - Fe_3O_4 reduction in the FR for 600–1000 °C and 1–6 bar is not observed. This is because Fe_2O_3 - Fe_3O_4 reduction is typically observed at a temperature range of 430 °C as compared to the FR temperature range of 600–1000 °C investigated in this work [62,63]. Nevertheless, both scenarios achieve maximum DR^+ at the lowest FR temperature of 600 °C. However, due to a transition between the reductive states in scenario 2, the DR^+ is eventually split at 0.51/0.27, 0.256/0.501, and 0.178/0.561 FeO/Fe for 800, 900, and 1000 °C, respectively. CaO reduction for CO_2 sequestration is only observed at 600 and 700 °C in both scenarios. During this period, the DR^+ decreases at 1.09–0.91 and 1.39–1.07 for scenarios 1 and 2, respectively. This corresponds to a period of a decrease in H_2 yield and an increase in CO_2 sequestration described elsewhere (3.1). This observation linked to the reduced DR of the LS in both instances might've contributed to a reaction shift described elsewhere in this work. Nevertheless, this could hint at the optimal temperatures of 600–700 °C for the carbonation phase during enhanced gasification.

The effects of the FR pressure on the DR^+ are shown in Fig. 7b. NiO is completely reduced to Ni at the minimum FR pressure of 1 bar while Fe_2O_3 only achieves a complete reduction at 5 bars. This means that the FR in scenario 2 must be maintained at pressures of 5 bar to achieve a competitive H_2 recovery and CO_2 sequestration while the FR in scenario 1 can be operated at reduced pressures and still be able to achieve a good H_2 yield. Moreover, carbonation in scenario 2 is observed to be more rapid than that in scenario 1. This is indicated by a steep DR curve in scenario 2 as compared to 1 which is further indicative of elevated CO_2 sequestration rates in the FR with pressure in 2 as compared to 1. This observation is reinforced by a steep CO_2 curve during 1–6 bar in scenario 1 as compared to 1 (Fig. 2b).

3.4. LS regeneration

In the present work, the degree of regeneration (DoR) for the solid carriers and CaO sorbent were evaluated at 700–900 °C, and 100–500 kg air/22.4 mol of Me_xO_y as shown in Fig. 7. The calciner reactor (CR) and air reactor (AR) pressures had no apparent effect and were maintained at 1 bar. Certain governing reactions for these are shown in R13 and R14. The depleted forms (DF) considered include Fe, FeO, Fe_3O_4 , and Ni, and CaCO_3 for Fe_2O_3 , NiO and CaO, respectively.

The DoR of the solid carriers with the temperature and aeration rate is shown in Fig. 2. It is noted that while these are presented in the same graphs, $\text{Me}_x\text{O}_{y-1}$ oxidation and CaCO_3 calcination occur separately in the AR and CR, respectively. Me_xO_y regeneration is influenced by the reactor temperatures and air supply while the regeneration of CaO is only influenced by the former. It is noted that the low-population-density (LPD) air is considered in this work and is restricted at 21 % O_2 and 79 % N_2 . It is further noted that the model bias in this analysis further negates the mechanical characteristics, linked to Me_xO_y attrition

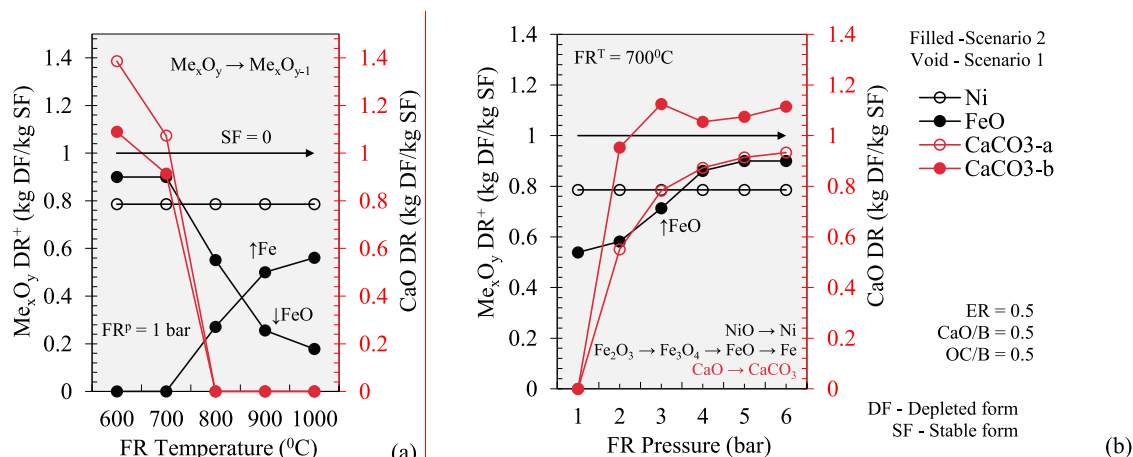


Fig. 7. The thermodynamic evolution of LS in the FR with a) Temperature of 600–1000 °C and b) Pressure of 1–6 bar.

and agglomeration during the successive cyclic reactions.

3.4.1. Calcination in CR

The degree of chemical dissociation of $CaCO_3$ in line with R14, was evaluated at 700–900 °C as shown in Fig. 8b. According to Fig. 8b, complete CaO regeneration is only possible from a CR temperature of 900 °C. This is presumably the optimal CR temperature for elevated CaO recovery during CL. At this temperature, a maximum CO_2 decoupling rate from $CaCO_3$ in both scenarios is observed at 513.2 and 341.7 kg/h in scenarios 1 and 2, respectively. For CR temperatures of 700 and 800 °C, the DR in both scenarios is observed to be consistent at 0.674 and 0.729 for scenarios 1 and 2, respectively. However, during this period, calcination in scenario 1 is less rapid than in scenario 2 with DR potentials at 0.729 and 0.647. This may be due to the different catalytic effects of the employed Me_xO_y in the separate scenarios described. Nonetheless, CO_2 decoupling in scenario 1 is observed to be more rapid than that in 2. This is due to a steep CO_2 output trajectory observed in scenario 1 as compared to 2. As such, at a maximum CR temperature of 9000C, scenario 1 achieves a maximum CO_2 decoupling of 513.98 kg/h as compared to that in scenario 2 at 341.71 kg/h. The different catalytic effects of the employed LS might have played a significant role in this observation. Consequently, a CO_2 -rich stream in both scenarios is

recovered for use in a lineated FT synthesis step.

3.4.2. Me_xO_{y-1} evolution in AR

The DR for both scenarios 1 and 2 with AR temperature and aeration rate is shown in Fig. 8a. Both scenarios achieve a complete Me_xO_y regeneration at the lowest AR temperature of 700 °C. However, during this period i.e., for AR temperatures of 700–900 °C., NiO regeneration is more rapid than that of Fe_2O_3 . This may be due to the multiple transitory state phases e.g., Fe_3O_4 , FeO , and Fe , incurred by the Fe_2O_3 OC during its evolution for reactivation as compared to NiO which undergoes a linear regenerative pathway from Ni . Additionally, the extent of RCC in both scenarios for temperatures of 700–900 °C is maintained and as such, considered complete. This indicates that the AR could be operated at the lowest AR temperature of 700 °C using either OC material to facilitate a complete OC oxidized state regeneration with maximum RCC efficiency.

For the aeration rate, however, the DR is observed to increase with air feed in both scenarios. In scenario 2, Me_xO_{y-1} oxidation to Me_xO_y is only observed at 200 kg air/22.4 mol Me_xO_y while that in scenario 1 is from the lowest employed aeration rate of 100 kg air/22.4 mol Me_xO_y . However, the rate of Me_xO_y regeneration in scenario 2 during the aeration period is observed to be more rapid than that in scenario 2.

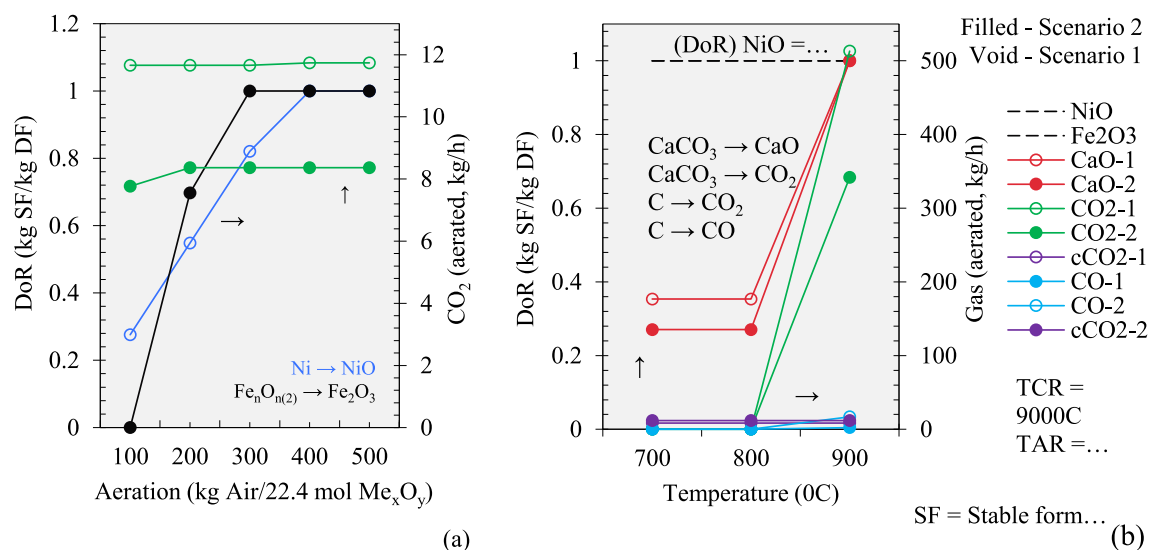


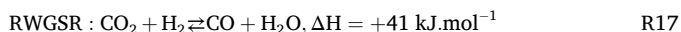
Fig. 8. The degree of regeneration with a) calciner reactor (CR) and air reactor (AR) temperature and b) Aeration rate in the air reactor AR.

Consequently, Fe_2O_3 achieves complete OC state regeneration at a lower air feed rate of 300 as compared to that of NiO at 400 amu. These compounding dissimilarities reported in this work for $\text{Me}_x\text{O}_{y-1}$ evolution in the AR with the air feed could also be linked to the different transitory $\text{Me}_x\text{O}_{y-1}$ phases incurred. However, more work studying these behaviors is needed to validate these assertions.

3.5. FT production

FT evaluation considers the influence of the RWGS temperature and pressure on the H_2/CO – R and CO_2 -x as shown in Fig. 9. Additionally, the FT product distributions, post-purification petroleum yields and related CO availability are shown. It also is noted that H_2 restricts the ASF-based petroleum potential in the Aspen Plus fixed conversion FTR model during R1-7.

The evaluation of the effects of the RWGS temperature and pressure on the synfuel R and x is shown. The RWGS facilitates a reverse R17 to leverage the use of the high-purity CO_2 S11 in compensating for the low levels of CO recovered in the syngas for a subsequent FT step. Certain governing reaction mechanisms employed in this reactor as well as end use-practicability are comprehensively described elsewhere [64–67]. The RWGSR is given in R21.



In the Aspen Plus RWGSR, the synfuel R decreases with increasing temperatures and pressures at 400–900 °C and 20–40 bar, respectively in both scenarios. This corresponds to a decrease in the CO_2 -x with the RWGS temperature and pressure in both scenarios. Consequently, a material tradeoff between the synfuel H_2 and CO_2 recovered in the flue gas with balance CO as shown in R21 is hinted. Thus, an elevated R and x for subsequent FT are obtained at reduced temperatures and pressures. These hint at optimal TF production capacities with a potentially tunable R with the RWGS temperature and pressure in both scenarios 1 and 2 for subsequent TF synthesis.

Regarding FT synthesis, a linked FT mapping is shown in 9c. FT components considered in Aspen Plus are indicated in Ref. [22]. The FT synthesis employed in this work considers carbon chains within C_n - C_{20} . Here, the CO availability and petroleum ($\text{C}_x\text{H}_y\text{O}_z$) yields were determined as shown in Eq (20) and (21). Nevertheless, $\text{C}_x\text{H}_y\text{O}_z$ recovery increases with the Petrofrac temperature while decreasing with the Petrofrac pressure of 1–150 °C and 1–40 bar, respectively, in both scenarios. During this period, CO availability decreases with the former while increasing with the latter. This is expected and may be due to $\text{C}_x\text{H}_y\text{O}_z$ synthesis being almost entirely dependent on CO availability in line with R1-R7 [68,69]. However, the low FT selectivity hinted by the Petrofrac yields may be linked to the low, wet-basis (in $\text{H}_2\text{O}_{(\text{F})}$) product selectivity potentials within 0.12 amu as shown in Fig. 9c. Nonetheless,

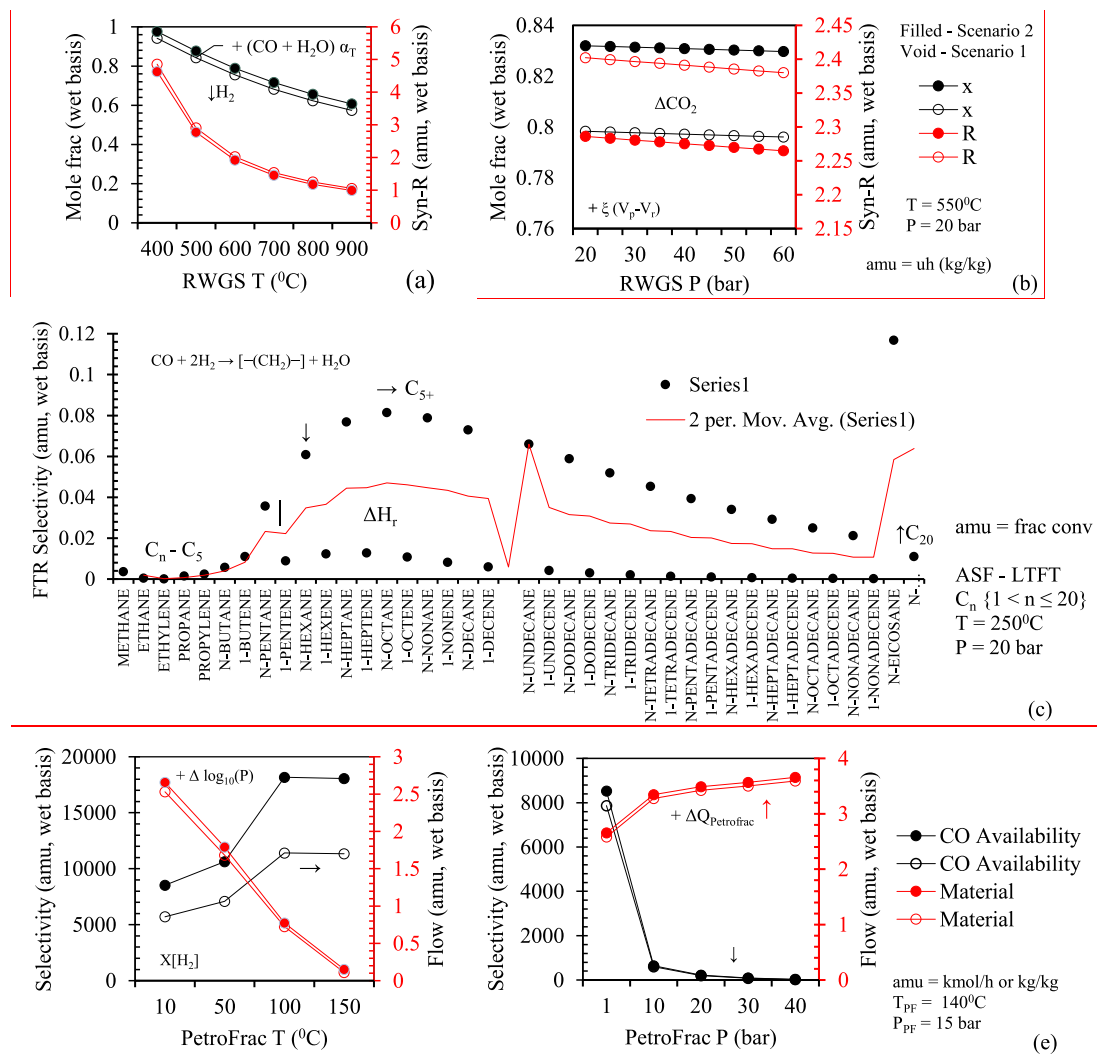


Fig. 9. FT synthesis a) Influence of RWGS temperature on the synfuel R and x b) Influence of RWGS pressure on the synfuel R and x c) FT distribution in FTR d) Influence of Petrofrac temperature on CO availability and FT yield and e) Influence of Petrofrac pressure on CO availability and FT yield.

These are due to the elevated amounts of $\text{H}_2\text{O}_{(\text{v})}$ produced when compared to the individual FT products during the ASF based FT synthesis [70]. Despite the OCs in scenarios 1 and 2, outlining comparable potentials for petroleum synthesis, the latter is observed to be slightly more efficient than the former for FT synthesis in terms of FT yield and CO availability. In fact, the FT yield in scenario 2 is consistently greater than that in scenario 1 for 1–150 °C and 1–40 bar. This may be due to elevated amounts of carbonaceous matter e.g. CO_2 , CO, CH_4 , available for conversion into more H_2 and CO in scenario 2 as compared to 1. Consequently, the overall FT yield in scenario 2 is observed to be higher than that in scenario 1. However, the eventual FT yields for petroleum recovery in both scenarios could be improved.

4. Conclusions

This study demonstrated the SECLG of waste bagasse to produce high-purity H_2 syngas and transportation fuels using high-performance NiO and Fe_2O_3 OCs. The results indicate that both OCs outline the highest potential for high-purity H_2 recovery of $\geq 68\%$ at the lowest FR temperature and pressures of 600 °C and 5 bar. The amount of generated CO_2 was found to be significantly limited to substantially less than 10 % of the producer gas in both scenarios. For the case of feed recirculation, it was observed that striking the right balance between reductive agents e.g., H_2O , Me_xO_y etc., and biomass quantities used is essential in delivering high-quality product gas. As such, optimal ER, RR, and CR of 1 CaO/dry fuel, $\leq 1 \text{ H}_2\text{O}_{(\text{v})}$ /dry fuel, and 0.2 Me_xO_y /dry fuel, respectively are proposed for high-purity H_2 syngas with near-zero CO_2 emissions. In terms of the producer gas quality, tar formation, gas composition, and energy content of the syngas were evaluated. The overall tar yield in the syngas was attained at low yields within 2×10^{-5} g/kg dry bagasse in both cases. Here, butane and ethane had the highest abundance as compared to naphthalene, phenanthrene, catechol, propane, and guaiacol. Further notable synfuel characteristics include elevated CH_4 and H_2O yields as compared to CO_2 and CO. These i.e., CH_4 and H_2O , roughly make up < 0.4 by molar fraction of the syngas in both cases. For the case of gas combustibility, at least 8480.53 cal per gm as minimum energy is embodied in the producer syngas for each scenario. Ultimately, the producer gas in both scenarios is effectively, and readily combustible. However, the maximum FCC of 27 % for both scenarios could be improved. The transportation fuel yield potential in both cases is promising owing to a tunable H_2/CO ratio obtained post a reverse water gas shift phase.

In terms of OC performance, NiO is observed to be more efficient than Fe_2O_3 in delivering high-purity H_2 syngas with increased CO_2 sequestration efficiencies at the lowest SECLG temperature and pressures of 600 °C and 1 bar. However, the latter OC gains superiority in delivering a producer gas blend with elevated combustibility potentials and higher FT petroleum over the former. While both OCs could be regenerated at the minimum AR temperature and aeration rate of 700 °C and 100 kg air/22.4 mol Me_xO_y , the regeneration of NiO was observed to be more rapid than that of Fe_2O_3 . Consequently, sufficient NiO could be regenerated at lower AR temperatures and feed rates to limit energy consumption as compared to Fe_2O_3 . High-purity H_2 production with minimal CO_2 output at low temperatures is a promising observation as it would significantly reduce the energy penalty incurred by existing gasification and lineated production technologies.

CRedit authorship contribution statement

Lebohlang Gerald Motsoeneng: Writing – original draft, Validation, Software, Methodology, Investigation. **Bilainu Oboirien:** Writing – review & editing, Supervision, Project administration, Methodology, Investigation, Funding acquisition, Conceptualization. **Andrea Lanzini:** Supervision.

Funding

The authors would like to thank the financial support from the University of Johannesburg Global Excellence and Stature (GES) 4.0 scholarship and National Research Foundation of South Africa.

Declaration of competing interest

The authors declare that they have no known competing financial interests or personal relationships that could have appeared to influence the work reported in this paper.

Appendix A. Supplementary data

Supplementary data to this article can be found online at <https://doi.org/10.1016/j.renene.2025.123022>.

References

- [1] H. Zhang, Z. Sun, Y.H. Hu, Steam reforming of methane: current states of catalyst design and process upgrading, *Renew. Sustain. Energy Rev.* 149 (2021) 111330.
- [2] R.G. dos Santos, A.C. Alencar, Biomass-derived syngas production via gasification process and its catalytic conversion into fuels by Fischer Tropsch synthesis: a review, *Int. J. Hydrogen Energy* 45 (36) (2020) 18114–18132.
- [3] M.M. Aba, I.L. Sauer, N.B. Amado, Comparative review of hydrogen and electricity as energy carriers for the energy transition, *Int. J. Hydrogen Energy* 57 (2024) 660–678.
- [4] D. Moodley, et al., Catalysis for sustainable aviation fuels: focus on fischer-tropsch catalysis, *Catal. Sustain. Environ.: React. Proc. Appl. Technol.* (2024) 73–116.
- [5] X. Zhao, et al., Biomass-based chemical looping technologies: the good, the bad and the future, *Energy Environ. Sci.* 10 (9) (2017) 1885–1910.
- [6] S.A. Rehman Khan, et al., Energy efficiency, carbon neutrality and technological innovation: a strategic move towards green economy, *Economic research-Ekonomska istraživanja* 36 (2) (2023).
- [7] N.M. Nguyen, et al., Biomass-based chemical looping gasification: overview and recent developments, *Appl. Sci.* 11 (15) (2021) 7069.
- [8] O. Condori, et al., Biomass chemical looping gasification for syngas production using ilmenite as oxygen carrier in a 1.5 kWth unit, *Chem. Eng. J.* 405 (2021) 126679.
- [9] X. Zhu, et al., Chemical looping beyond combustion—a perspective, *Energy Environ. Sci.* 13 (3) (2020) 772–804.
- [10] I. Martínez Berge, et al., Optimised Production of Tailored Syngas from Municipal Solid Waste (MSW) by sorption-enhanced Gasification, 2020.
- [11] X. Wang, et al., Prediction of In-Situ gasification chemical looping combustion effects of operating conditions, *Catalysts* 8 (11) (2018) 526.
- [12] G. Liu, et al., Hydrogen and power co-production from autothermal biomass sorption enhanced chemical looping gasification: thermodynamic modeling and comparative study, *Energy Convers. Manag.* 269 (2022) 116087.
- [13] T. Detchusanarand, et al., Analysis of the sorption-enhanced chemical looping biomass gasification process: performance assessment and optimization through design of experiment approach, *Energy* 207 (2020) 118190.
- [14] X. Wang, et al., Modelling and optimization of sorption-enhanced biomass chemical looping gasification coupling with hydrogen generation system based on neural network and genetic algorithm, *Chem. Eng. J.* 473 (2023) 145303.
- [15] S. Wang, et al., Performance of sorption-enhanced chemical looping gasification system coupled with solid oxide fuel cell using exergy analysis, *Int. J. Hydrogen Energy* 46 (2) (2021) 1752–1761.
- [16] B. Li, et al., Thermodynamic evaluation of sorption-enhanced chemical looping gasification with coal as fuel, *Int. J. Hydrogen Energy* 45 (41) (2020) 21186–21194.
- [17] M. Osat, F. Shojaati, M. Osat, Techno-economic assessment of butanol and pentanol productions from sorption enhanced chemical looping gasification of a lignocellulosic biomass, *Renew. Energy* 217 (2023) 119176.
- [18] D. Li, et al., Chemical looping conversion of gaseous and liquid fuels for chemical production: a review, *Energy Fuel* 34 (5) (2020) 5381–5413.
- [19] P. Aryal, A. Tanksale, A. Hoadley, Oxidative catalytic steam gasification of sugarcane bagasse for hydrogen rich syngas production, *Int. J. Hydrogen Energy* 48 (40) (2023) 15014–15025, 8 May 2023.
- [20] E.Y. Kombe, et al., Process modeling and evaluation of optimal operating conditions for production of hydrogen-rich syngas from air gasification of rice husks using aspen plus and response surface methodology, *Bioresour. Technol.* 361 (2022) 127734.
- [21] P. Hosseini, S. Jamshidi, An evolved cubic equation of state with a new attractive term, *Fluid Phase Equilib.* 408 (2016) 58–71.
- [22] I.P. Silva, et al., Development of a semi-empirical model for woody biomass gasification based on stoichiometric thermodynamic equilibrium model, *Energy* 241 (2022) 122894.
- [23] P. Aryal, A. Tanksale, A. Hoadley, Oxidative catalytic steam gasification of sugarcane bagasse for hydrogen rich syngas production, *Int. J. Hydrogen Energy* 48 (40) (2023) 15014–15025.

- [24] A.S. Noushabadi, et al., Estimation of higher heating values (HHVs) of biomass fuels based on ultimate analysis using machine learning techniques and improved equation, *Renew. Energy* 179 (2021) 550–562.
- [25] E.-C. Yang, et al., Semi-empirical PM3 study upon the complexation of β -cyclodextrin with 4, 4'-benzidine and o-tolidine, *J. Mol. Struct.: THEOCHEM* 712 (1–3) (2004) 75–79.
- [26] R. Barker, The reversibility of the reaction $\text{CaCO}_3 \rightleftharpoons \text{CaO} + \text{CO}_2$, *J. Appl. Chem. Biotechnol.* 23 (10) (1973) 733–742.
- [27] B. Bulfin, et al., Intensification of the reverse water–gas shift process using a countercurrent chemical looping regenerative reactor, *Chem. Eng. J.* 461 (2023) 141896.
- [28] D. Selvatico, A. Lanzini, M. Santarelli, Low Temperature Fischer-Tropsch fuels from syngas: kinetic modeling and process simulation of different plant configurations, *Fuel* 186 (2016) 544–560.
- [29] J.A. Okolie, et al., Hydrothermal gasification of soybean straw and flax straw for hydrogen-rich syngas production: experimental and thermodynamic modeling, *Energy Convers. Manag.* 208 (2020) 112545.
- [30] L.P.R. Pala, et al., Steam gasification of biomass with subsequent syngas adjustment using shift reaction for syngas production: an aspen plus model, *Renew. Energy* 101 (2017) 484–492.
- [31] A. Porcu, et al., Experimental validation of a multiphase flow model of a lab-scale fluidized-bed gasification unit, *Appl. Energy* 293 (2021) 116933.
- [32] H. Shafiq, S.U. Azam, A. Hussain, Steam gasification of municipal solid waste for hydrogen production using aspen plus® simulation, *Discover Chem. Eng.* 1 (2021) 1–16.
- [33] R. Tavares, et al., Numerical investigation of optimum operating conditions for syngas and hydrogen production from biomass gasification using Aspen plus, *Renew. Energy* 146 (2020) 1309–1314.
- [34] V. Rehnberg, High-Throughput in-silico Screening of Oxygen Carrier Candidates for Chemical Looping Oxygen uncoupling-thermodynamical and Practical Considerations of Data Mining from ab-initio Databases—Towards a cost-effective Negative Emission Technology, 2020.
- [35] K. Wang, Q. Yu, Q. Qin, The thermodynamic method for selecting oxygen carriers used for chemical looping air separation, *J. Therm. Anal. Calorim.* 112 (2013) 747–753.
- [36] M.N. Khan, T. Shamim, Thermodynamic screening of suitable oxygen carriers for a three reactor chemical looping reforming system, *Int. J. Hydrogen Energy* 42 (24) (2017) 15745–15760.
- [37] S. Dey, N. Mehta, Oxidation of carbon monoxide over various nickel oxide catalysts in different conditions: a review, *Chem. Eng. J. Adv.* 1 (2020) 100008.
- [38] P. Azadi, et al., Interactions of supported nickel and nickel oxide catalysts with methane and steam at high temperatures, *Chem. Eng. Sci.* 66 (18) (2011) 4196–4202.
- [39] I. Samprón, et al., Biomass chemical looping gasification of pine wood using a synthetic $\text{Fe}_2\text{O}_3/\text{Al}_2\text{O}_3$ oxygen carrier in a continuous unit, *Bioresour. Technol.* 316 (2020) 123908.
- [40] P. Prasertcharoensuk, S.J. Bull, A.N. Phan, Gasification of waste biomass for hydrogen production: effects of pyrolysis parameters, *Renew. Energy* 143 (2019) 112–120.
- [41] C. Zhang, et al., Thermodynamic analysis of integrated sorption-enhanced staged-gasification of biomass and in-situ CO_2 utilization by methane reforming process based on calcium looping, *Energy Convers. Manag.* 278 (2023) 116710.
- [42] F. Meng, J. Meng, D. Zhang, Influence of higher equivalence ratio on the biomass oxygen gasification in a pilot scale fixed bed gasifier, *J. Renew. Sustain. Energy* 10 (5) (2018).
- [43] A.M. Shakorforow, Operating and performance gasification process parameters, *Int. J. Sci. Res.* 5 (6) (2016) 1768–1775.
- [44] V. Kirsanovs, et al., The influence of process temperature, equivalence ratio and fuel moisture content on gasification process: a review, in: *Proceedings of the 27th International Conference on Efficiency, Cost, Optimization, Simulation and Environmental Impact of Energy Systems—Ecos*, Turku, 2014. Finland.
- [45] R.-Y. Chein, W.-H. Hsu, Thermodynamic equilibrium analysis of H_2 -rich syngas production via sorption-enhanced chemical looping biomass gasification, *Renew. Energy* 153 (2020) 117–129.
- [46] Y. Wu, et al., Syngas production by chemical looping gasification of biomass with steam and CaO additive, *Int. J. Hydrogen Energy* 43 (42) (2018) 19375–19383.
- [47] O. Condori, et al., Parametric evaluation of clean syngas production from pine forest residue by chemical looping gasification at the 20 kWth scale, *J. Clean. Prod.* (2023) 140434.
- [48] X.A. Garcia, K.J. Hüttinger, Steam gasification of naphthalene as a model reaction of homogeneous gas/gas reactions during coal gasification, *Fuel* 68 (10) (1989) 1300–1310.
- [49] M. Vaezi, et al., Gasification of heavy fuel oils: a thermochemical equilibrium approach, *Fuel* 90 (2) (2011) 878–885.
- [50] S. Suryawanshi, et al., Parametric study of different biomass feedstocks used for gasification process of gasifier—a literature review, *Biomass Convers. Biorefin.* 13 (9) (2023) 7689–7700.
- [51] H. Gu, et al., Study on biomass gasification under various operating conditions, *J. Energy Inst.* 92 (5) (2019) 1329–1336.
- [52] A.A. Ahmad, et al., Assessing the gasification performance of biomass: a review on biomass gasification process conditions, optimization and economic evaluation, *Renew. Sustain. Energy Rev.* 53 (2016) 1333–1347.
- [53] Z. Huang, et al., Thermodynamic analysis and thermogravimetric investigation on chemical looping gasification of biomass char under different atmospheres with Fe_2O_3 oxygen carrier, *Appl. Energy* 157 (2015) 546–553.
- [54] M.P. Bracciale, et al., Clean syngas and hydrogen Co-Production by gasification and chemical looping hydrogen process using MgO-Doped Fe_2O_3 as redox material, *Catalysts* 12 (10) (2022) 1273.
- [55] V. Marcantonio, et al., Modelling and assessment of a sorption enhanced gasification system coupled with hydrothermal carbonization, hot gas cleaning, and plasma to produce pure H_2 from biomass, *Int. J. Hydrogen Energy* 48 (84) (2023) 32672–32685.
- [56] I. Martínez, et al., Experimental investigation on sorption enhanced gasification (SEG) of biomass in a fluidized bed reactor for producing a tailored syngas, *Fuel* 259 (2020) 116252.
- [57] P. Leung, et al., Raising the fuel heating value and recovering exhaust heat by on-board oxidative reforming of bioethanol, *Energy Environ. Sci.* 3 (6) (2010) 780–788.
- [58] G. Del Alamo, et al., Characterization of syngas produced from MSW gasification at commercial-scale ENERGOS plants, *Waste Manag.* 32 (10) (2012) 1835–1842.
- [59] Y.-L. Zhang, et al., Reduction mechanism of $\text{Fe}_2\text{O}_3\text{-Cr}_2\text{O}_3\text{-NiO}$ system by carbon, *J. Cent. S. Univ.* 23 (6) (2016) 1318–1325.
- [60] Y. Zhang, et al., Reduction of Fe and Ni in Fe-Ni-O systems, *J. Min. Metall. B Metall.* 49 (1) (2013) 13–20.
- [61] K. Abdel-Halim, et al., Carbothermic reduction kinetics of nanocrystallite $\text{Fe}_2\text{O}_3/\text{NiO}$ composites for the production of Fe/Ni alloy, *J. Alloys Compd.* 463 (1–2) (2008) 585–590.
- [62] B. Huang, Y. Liu, Z. Tan, Discovery of a low-temperature Fe_2O_3 reduction route to Fe with carbon via Fe-MOF-74 decomposition, *Chem. Commun.* 58 (80) (2022) 11296–11299.
- [63] M. Bohra, Wet H_2 reduction: a robust way of converting $\alpha\text{-Fe}_2\text{O}_3$ into Fe_3O_4 at the nanoscale, *J. Electron. Mater.* 51 (6) (2022) 2709–2715.
- [64] M. González-Castaño, B. Dorneanu, H. Arellano-García, The reverse water gas shift reaction: a process systems engineering perspective, *React. Chem. Eng.* 6 (6) (2021) 954–976.
- [65] A. Wolf, A. Jess, C. Kern, Syngas production via reverse water-gas shift reaction over a Ni- Al_2O_3 catalyst: catalyst stability, reaction kinetics, and modeling, *Chem. Eng. Technol.* 39 (6) (2016) 1040–1048.
- [66] H. Kirsch, et al., Power-to-fuel conversion based on reverse water-gas-shift, fischer-tropsch synthesis and hydrocracking: mathematical modeling and simulation in matlab/simulink, *Chem. Eng. Sci.* 227 (2020) 115930.
- [67] E. Pahija, et al., Experimental and computational synergistic design of Cu and Fe catalysts for the reverse water–gas shift: a review, *ACS Catal.* 12 (12) (2022) 6887–6905.
- [68] C. Niu, et al., A hybrid kinetics integrating feed-consumption rate and product selectivity models for fischer-tropsch synthesis over an industrial cobalt-based catalyst, *Chem. Eng. J.* 455 (2023) 140817.
- [69] R. Guettel, T. Turek, Comparison of different reactor types for low temperature fischer-tropsch synthesis: a simulation study, *Chem. Eng. Sci.* 64 (5) (2009) 955–964.
- [70] G. Zang, et al., Performance and cost analysis of liquid fuel production from H_2 and CO_2 based on the fischer-tropsch process, *J. CO₂ Util.* 46 (2021) 101459.